J. Fluid Mech. (1976), *vol.* 76, *part* 2, *pp.* 229–250
Printed in Great Britain

The growth of gravity–capillary waves in a coupled shear flow

By G. R. VALENZUELA

Ocean Sciences Division, Naval Research Laboratory, Washington D.C. 20375

(Received 19 August 1975 and in revised form 24 February 1976)

The growth rates and phase speeds of gravity–capillary wind waves are investigated through numerical solution of a linear, viscous, coupled, shear-flow perturbation model. Numerical results are obtained by transforming the boundary-value problem of a perturbed mean laminar shear flow into a matrix-eigenvalue problem using standard finite-difference methods.

Detailed calculations are performed for a basic state composed of a logarithmic–linear mean flow profile in the air and a linear–logarithmic mean flow profile in the water. We exclude turbulent Reynolds stresses. Calculated growth rates show excellent agreement with corresponding experimental growth rates. This implies that the initial growth of gravity–capillary wind waves is almost certainly due to the instability of the coupled laminar shear flow in the air and water.

The investigation also demonstrates that the shear flow in the water cannot be ignored in wave growth studies, since the usual 3–4 %, highly sheared, wind-induced surface drift produces a significant increase in the growth of wind-generated gravity–capillary waves.

1. Introduction

A major advance towards reliable ocean wave prediction has been made in recent years by Hasselmann *et al.* (1973). This work demonstrates the dominant role of wave–wave interactions in shaping the wave spectrum during its development. Nonetheless the identity of the mechanisms responsible for transfer of momentum and energy from wind to waves has not been firmly established. Phillips (1966, pp. 79–87) considers growth arising from resonant interaction of water waves with turbulent fluctuations in the air. Miles (1957, 1959) considers the effect of a laminar shear flow in the air alone on wave growth. A phase-shifted pressure at a critical layer where the wave and air speeds coincide enters the theory. Neither of these theories agrees with experiment. The results of Miles's (1962*b*) subsequent perturbation of the viscous boundary layer yielded more reasonable growth rates for gravity–capillary waves, but results of experimental comparisons (Stewart 1970; Gottifredi & Jameson 1970; Wilson *et al.* 1973) were equivocal and limited to very low wind speeds and to waves so long that the approximations of Miles's (1962*b*) calculations were not clearly valid.

Recently Larson & Wright (1975) measured initial growth rates using a microwave radar technique which permitted them to treat shorter waves and higher wind speeds. Comparison of Miles's (1962*b*) predictions with these latest measure-

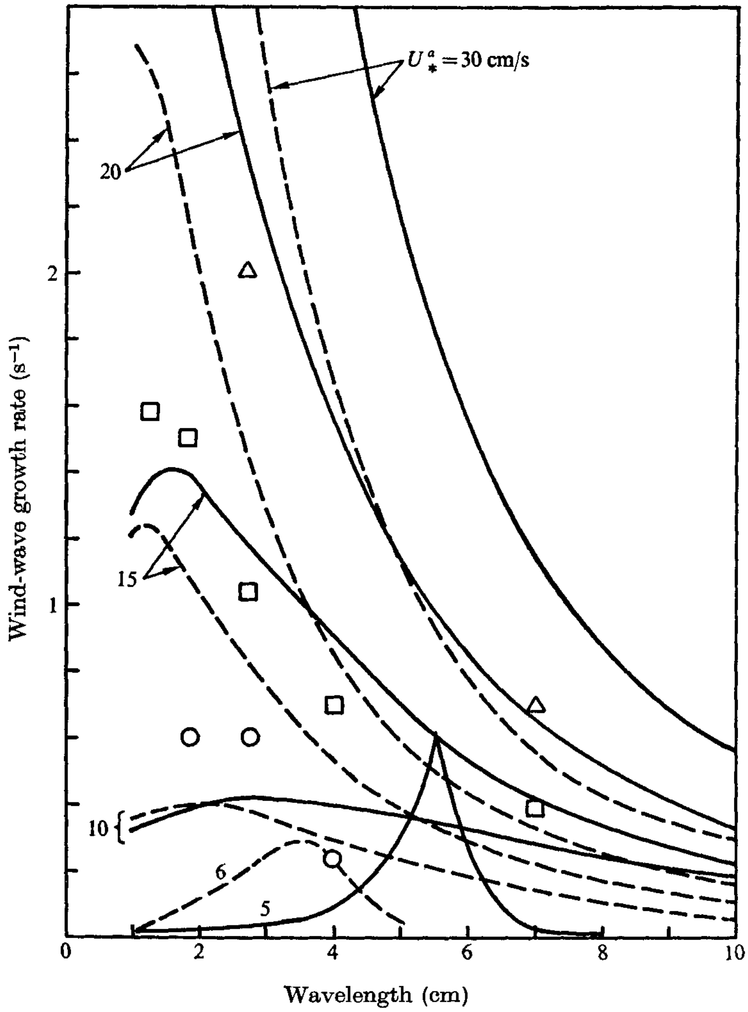

FIGURE 1. Comparison of measured wind-wave growth rates and Miles's (1962*b*) predictions. Miles's theory: ——, $U_1^a = 8U_*^a$; – – –, $U_1^a = 5U_*^a$. Experiment (Larson & Wright): ○, $U_*^a = 7$ cm/s; □, $U_*^a = 15$ cm/s; △, $U_*^a = 27$ cm/s.

ments (figure 1) strongly supports Miles's (1962*b*) basic procedure. Miles did not include the shear flow in the water in his calculations; it is known that the phase speed of wind waves in the gravity–capillary region depends on the wind-induced drift in the water (Wright & Keller 1971; Shemdin 1972). Thus, in reality it is the coupled shear flow, including the wind drift, which should be perturbed to obtain growth rates. Furthermore, Miles (1962*b*) used Benjamin's (1959) approximate boundary conditions and generally relied on the decomposition of the solution of the Orr–Sommerfeld equation into inviscid and viscous parts. This dichotomy is valid as long as the thickness of the viscous boundary layer, of order ν/U_*, is large compared with the critical-layer (friction-layer) thickness $(\nu/kU')^{\frac{1}{3}}$. It is seen in figure 2 that this condition is satisfied only at larger wavenumbers and

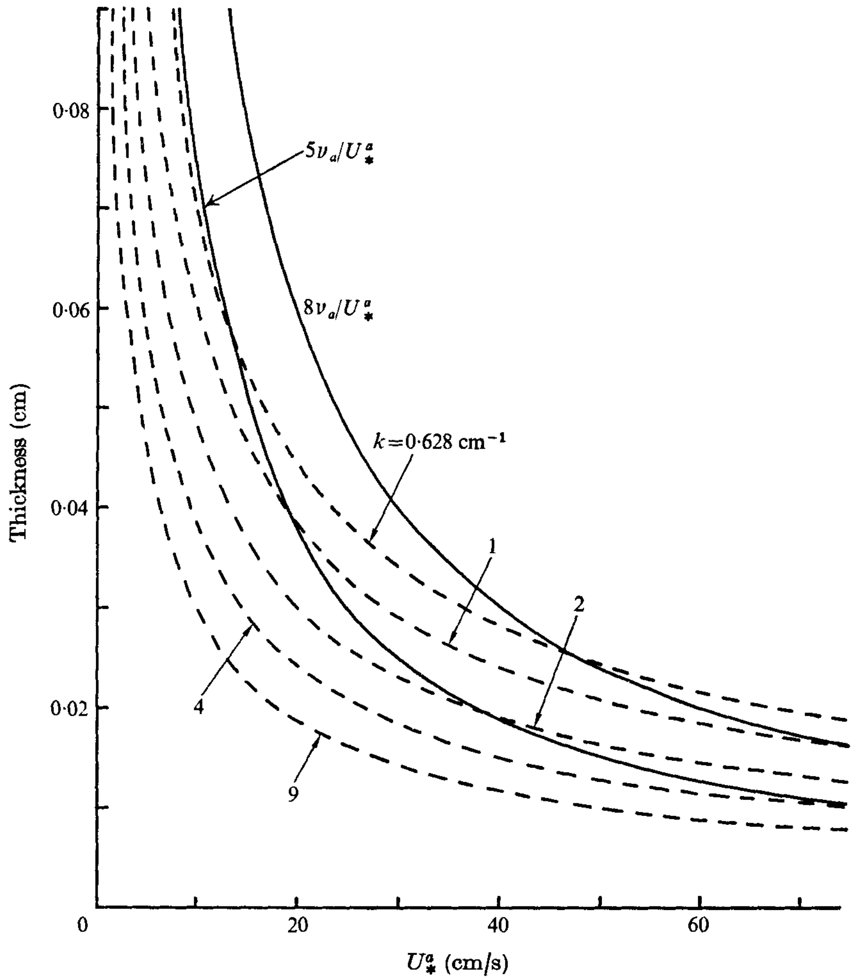

FIGURE 2. Boundary-layer thickness (solid curves) and critical-layer thickness (dashed curves) as a function of air friction velocity. ν_a is the kinematic viscosity of the air and U_*^a is the air friction velocity.

for the smaller air friction velocities (i.e. small wind speeds). It is the purpose of this work to extend Miles's results to higher wind speeds by numerical solution of the Orr–Sommerfeld eigenvalue problem as well as to determine the extent to which the flow in the water (the wind drift) affects the wave growth rates.

The formal development of the linear, coupled, shear-flow perturbation model has been given by Keller, Larson & Wright (1974) but results were obtained only from an uncoupled version of the model from which the flow in the air was essentially excluded. This uncoupled model predicted realistic phase speeds, but incorrectly yielded a growing wave travelling against the wind and a decaying wave travelling with the wind. Previously, Shemdin (1972), using an inviscid form of the coupled shear-flow model, obtained phase speeds that were in qualitative agreement with experimental results, but did not include viscosity.

In §2 the coupled shear-flow perturbation model with a harmonic disturbance on the surface is developed starting from the Navier–Stokes differential equation for incompressible fluid flow. Linearization of the differential equations and elimination of the pressure yields the Orr–Sommerfeld differential equation for the vertical dependence of the first-order stream function of the flow. The flows in the air and in the water are connected through the continuity of velocity and stress components at the free surface. In §3 well-established finite-difference techniques are introduced for solving the Orr–Sommerfeld differential equation. These methods have been used by Thomas (1953), Kurtz & Crandall (1962), Osborne (1967), Jordinson (1970) and Hughes (1972), among others, to treat plane Poiseuille and Blasius laminar shear flows over a rigid boundary. Here Osborne's (1967) iterative scheme is adopted to deal with our more complex boundary-value problem involving a logarithmic–linear mean flow profile in the air and a linear–logarithmic profile in the water. The numerical results are presented in §4. This iterative scheme, which uses a uniform grid spacing for the vertical variable z, Numerov transformation and Gaussian matrix inversion, works best for small wind speeds and large wavenumbers (i.e. towards 8·67 cm^{-1}). Convergence of the eigenvalues (i.e. complex phase speeds) is obtained in three to four iterations in most cases. For the higher wind speeds (i.e. greater than 6 m/s) the critical layer, present in the air for the mode travelling with the wind, descends towards the air–water interface and convergence is not achieved as readily for the smaller wavenumbers. The coupled shear-flow model correctly yields a growing wave travelling with the wind and a decaying wave travelling against the wind.

In §5 the growth rates obtained with the coupled shear-flow model are compared with the Miles (1962*b*) predictions and with experimental measurements. The comparison with Miles indicates that the uncoupled model may underestimate the growth rates for the small wavenumbers (i.e. less than 1·55 cm^{-1}) and may somewhat overestimate the growth for the larger wavenumbers. The comparison of measured and theoretical growth rates shows reasonable agreement in magnitude and in dependence upon the air friction velocity. In fact at the largest wavenumber examined, 8·67 cm^{-1}, the agreement is quite remarkable. The inclusion of the wind drift yields growth rates at smaller wavenumbers which are significantly greater than those predicted when the flow in the water is neglected.

We believe that this agreement implies that the growth of gravity–capillary waves is indeed due to linear instability of the coupled shear flow at the air–water interface. Larson & Wright (1975) have noted that the magnitude of the measured growth rates is such that the entire wind stress can be supported by the short waves. Thus it is not necessary to assume the existence of turbulent, wave-induced Reynolds stresses, air-flow separation or other nonlinear features of the air flow in order to explain the transfer of momentum from wind to waves.

2. Formulation of the model

Consider an established mean laminar shear flow $U(z)$ in the air and in the water. A harmonic disturbance (gravity–capillary wave) travels with or against the wind at the phase speed $\mathrm{Re}(c)$ on the air–water interface (figure 3). We seek the growth or damping rate and phase speed of this surface wave. The flow in the air and in the water can be described by the Navier–Stokes equation for an incompressible fluid flow **W**:

$$\partial \mathbf{W}/\partial t + (\mathbf{W}.\nabla)\,\mathbf{W} + \rho^{-1}\nabla\mathscr{P} - \nu\nabla^2\mathbf{W} = 0, \tag{2.1}$$

where ρ is the density of the fluid, ν is the kinematic viscosity of the fluid, $\mathscr{P}$ is the total pressure and t is time. We take x as the horizontal co-ordinate and z as the vertical co-ordinate. At $z = \pm\infty$ the vertical component of velocity must vanish, and at the air–water interface the normal and tangential velocity and stress components must be continuous. In our approximation the total flow **W** is composed of an established laminar shear flow $(U(z), 0)$ (i.e. the flow which would be present in the absence of the harmonic disturbance) and a first-order flow $(u(x,z;t), w(x,z;t))$ described by the linearized form of (2.1) when the surface wave is present (the expansion parameter is the slope of the surface wave). Similarly the total pressure $\mathscr{P}$ is composed of the static pressure $P(z)$ and a first-order pressure $p(x,z;t)$ due to the harmonic disturbance, where

$$p(x,z;t) = p(z)\exp\,[ik(x-ct)]. \tag{2.2}$$

For convenience the first-order flow is to be derived from a stream function $\psi(x,z;t) = \phi(z)\,\exp\,[ik(x-ct)]$, where k is the wavenumber of the surface wave and c is the complex eigenvalue of our boundary-value problem. The real part of c is the phase speed and the imaginary part of c is related to the growth or damping of the surface wave. Eliminating the first-order pressure from the linearized Navier–Stokes equation yields the well-known Orr–Sommerfeld differential equation. Thus, in the air $\phi(z)$ must satisfy

$$i\nu_a(\phi_a^{\mathrm{iv}} - 2k^2\phi_a'' + k^4\phi_a) + k[(U-c)(\phi_a'' - k^2\phi_a) - U_a''\phi_a] = 0 \tag{2.3}$$

whereas in the water $\phi(z)$ satisfies

$$i\nu_w(\phi_w^{\mathrm{iv}} - 2k^2\phi_w'' + k^4\phi_w) + k[(U-c)(\phi_w'' - k^2\phi_w) - U_w''\phi_w] = 0, \tag{2.4}$$

where the subscripts a and w refer to the air and water respectively, and the primes signify derivatives with respect to the variable z.

The first-order wave pressure in each medium can be obtained from the horizontal component of the linearized Navier–Stokes equation. Thus, in the air

$$\rho_a^{-1}p_a(z) = -(U-c)\phi_a' + U_a'\phi_a - ik^{-1}\nu_a(\phi_a''' - k^2\phi_a') - g\xi \tag{2.5}$$

and in the water

$$\rho_w^{-1}p_w(z) = -(U-c)\phi_w' + U_w'\phi_w - ik^{-1}\nu_w(\phi_w''' - k^2\phi_w') - g\xi, \tag{2.6}$$

where the wave pressures are departures from hydrostatic, g is the acceleration due to gravity and the first-order surface displacement is

$$\zeta(x;t) = \xi\exp\,[ik(x-ct)].$$

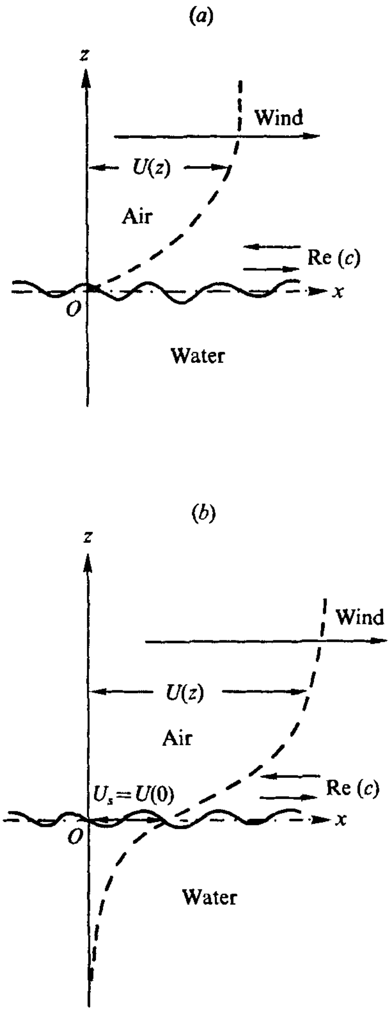

FIGURE 3. Illustration of coupled shear flows in the air and in the water. On the surface a harmonic disturbance (wave) travels with the wind or against the wind. (*a*) Loglin–zero profile. (*b*) Loglin–linlog profile.

At the free surface the discontinuity in normal prersure must be balanced by surface tension and the tangential stress must be continuous. The boundary conditions are applied at the free surface but are referred to $z = 0$ by using a Taylor expansion (Phillips 1966, p. 24). At first order this is equivalent to Benjamin's (1959) use of curvilinear co-ordinates for the flow. Accordingly, the first-order continuity condition for the normal pressure is

$$-p_w(z) + 2\mu_w \frac{\partial w_w}{\partial z} + p_a(z) - 2\mu_a \frac{\partial w_a}{\partial z} = T' \frac{\partial^2 \zeta}{\partial x^2}, \tag{2.7}$$

where μ_w and μ_a are the (molecular) viscosity coefficients of water and air respectively, and T' is the surface tension of the interface.

To first order, continuity of tangential stress at the free surface yields

$$\mu_a\left(\frac{\partial w_a}{\partial x}+\frac{\partial u_a}{\partial z}+\zeta\frac{\partial^2 U_a}{\partial z^2}\right)=\mu_w\left(\frac{\partial w_w}{\partial x}+\frac{\partial u_w}{\partial z}+\zeta\frac{\partial^2 U_w}{\partial z^2}\right)\quad \text{at}\quad z=0. \tag{2.8}$$

The continuity of the first-order velocity components at the free surface requires that

$$\left.\begin{aligned} w_a &= w_w \qquad &(2.9)\\ u_a+\zeta\frac{\partial U_a}{\partial z} &= u_w+\zeta\frac{\partial U_w}{\partial z} \qquad &(2.10)\end{aligned}\right\}\quad \text{at}\quad z=0.$$

Hence, combining (2.5)–(2.7), using the stream function to describe the velocities and introducing the kinematic boundary condition $\xi=-\phi/(U_s-c)$ (i.e. $U_s=U(0)$) we obtain the boundary condition for the normal pressure at $z=0$:

$$\begin{aligned}&\rho_a[(U_s-c)^2k\phi_a'-k(U_s-c)U_a'\phi_a+i\nu_a(U_s-c)(\phi_a'''-3k^2\phi_a')-gk\phi_a]\\ &\quad=\rho_w[(U_s-c)^2k\phi_w'-k(U_s-c)U_w'\phi_w+i\nu_w(U_s-c)(\phi_w'''-3k^2\phi_w')-(gk+Tk^3)\phi_w],\end{aligned} \tag{2.11}$$

where $T=T'/\rho_w$.

Similarly, the other boundary conditions (2.8)–(2.10) may be reduced to

$$\mu_a[(U_s-c)(\phi_a''+k^2\phi_a)-U_a''\phi_a]=\mu_w[(U_s-c)(\phi_w''+k^2\phi_w)-U_w''\phi_w], \tag{2.12}$$

$$\phi_a=\phi_w \tag{2.13}$$

and

$$(U_s-c)\phi_a'-U_a'\phi_a=(U_s-c)\phi_w'-U_w'\phi_w, \tag{2.14}$$

respectively, at $z=0$.

The boundary conditions at $z=\pm\infty$ for the first-order flow are

$$\phi\exp(\pm kz)\rightarrow\text{constant}. \tag{2.15}$$

Therefore the boundary-value problem to be solved for the eigenvalue reduces to the pair of Orr–Sommerfeld equations (2.3) and (2.4) for the flow in the air and in the water together with the boundary conditions (2.11)–(2.14) at $z=0$ and the boundary conditions (2.15) at $z=\pm\infty$. Exact analytic solution of this problem is out of the question. Therefore, in the following section we shall use finite-difference methods to solve this problem numerically.

3. Finite-difference methods

Finite-difference methods for solving the Orr–Sommerfeld differential equation have been developed for plane Poiseuille flow by Thomas (1953) and Hughes (1972) and for Blasius laminar flow over a flat surface by Kurtz & Crandall (1962), Osborne (1967) and Jordinson (1970), among others. In our case we deal with an established mean flow profile in two different media: a logarithmic–linear profile in the air and a linear–logarithmic profile in the water. The boundary conditions at the free surface connecting the shear flows are considerably more complex than those used in the previous investigations.

The Orr–Sommerfeld equations and the boundary conditions for the flows are approximated by finite-difference expressions and the resulting eigenvalue problem can be solved by standard matrix-inversion techniques. To approximate the Orr–Sommerfeld differential equation as accurately as possible, we draw upon previous work and introduce the Numerov transformation (Osborne 1967). Accordingly, we let

$$\phi = (1+\tfrac{1}{6}\delta^2-\tfrac{1}{720}\delta^4)\theta, \tag{3.1}$$

where δ^2 and δ^4 are standard central-difference notation. If D denotes d/dz and h is the increment in z, then $\delta^2 = (hD)^2$ and $\delta^4 = (hD)^4$. The Orr–Sommerfeld equation in finite-difference form for the more accurate variable θ is

$$\begin{aligned}\{i\nu[\delta^4-2k^2h^2(\delta^2+\tfrac{1}{12}\delta^4)+k^4h^4(1+\tfrac{1}{6}\delta^2)]+h^2k(U-c)[\delta^2+\tfrac{1}{12}\delta^4 \\ -h^2k^2(1+\tfrac{1}{6}\delta^2)]-kh^4U''(1+\tfrac{1}{6}\delta^2-\tfrac{1}{720}\delta^4)\}\theta = 0.\end{aligned} \tag{3.2}$$

The term in δ^4 in the coefficient of U'' has been dropped in the numerical calculations since it is of higher order than our truncation error.

The finite-difference equation (3.2) is then explicitly written out for each level $z = nh$ in the air and each level $z = -nh$ in the water, for $n = 0, 1, 2, \ldots, N$. Following Osborne (1967) and Jordinson (1970) the finite-difference expressions $\delta^2, \delta^4, \mu\delta = hD$ and $\mu\delta^3 = (hD)^3$ also needed in the boundary conditions are developed to fourth order in h. The Orr–Sommerfeld equation in finite-difference form at each level z requires the value of the eigenfunction θ at five consecutive levels. In symbolic notation, (3.2) is of the form

$$A_p\theta_{p+2}+B_p\theta_{p+1}+C_p\theta_p+B_p\theta_{p-1}+A_p\theta_{p-2} = 0, \tag{3.3}$$

where $\theta_p = \theta(z = ph)$, $\theta_{p+1} = \theta(z = (p+1)h)$, $\theta_{p-1} = \theta(z = (p-1)h)$ and so forth. Thus, when the finite-difference approximation to the Orr–Sommerfeld equation is written down for $z = \pm 2h$, $\pm h$ and 0, the fictitious values θ^a_{-2}, θ^a_{-1}, θ^w_{+1} and θ^w_{+2} appear. In our case θ^w_0 is also an extra quantity since we use θ^a_0 at $z = 0$ in the system of equations. To eliminate the four fictitious values of θ and the unwanted value θ^w_0 use is made of the four boundary conditions (2.11)–(2.14) in finite-difference form, together with the finite-difference form of the Orr–Sommerfeld equation at $z = 0$ on the water side. We also let $U''_a(0) = U''_w(0) = 0$ in (2.12) since it is assumed that boundary layers are always present at the air–water interface. At $z = \pm Nh \equiv \pm z_{\max}$ and at $z = \pm(N-1)h$ we have used the boundary conditions (2.15), which in finite-difference form are

$$\theta_{\pm(N+2)} = \exp(\mp 2kh)\theta_{\pm N}, \quad \theta_{\pm(N+1)} = \exp(\mp kh)\theta_{\pm N}. \tag{3.4}$$

After algebraic manipulation the unwanted values of the eigenfunction can be obtained in terms of the desired values θ^a_0, θ^a_1, θ^a_2, θ^w_{-1} and θ^w_{-2}. The resultant matrix-eigenvalue problem to be solved for c is of the form

$$\mathscr{M}(c)\mathbf{v} = 0, \tag{3.5}$$

where $\mathscr{M}(c)$ is a multidiagonal matrix which contains a principal diagonal band of nine non-zero elements. The matrix turns out to be asymmetric about the main diagonal because of the manner in which the boundary conditions are included in the finite-difference expression for the Orr–Sommerfeld equation. Note that in the case of the uncoupled shear flow over a rigid boundary (Osborne 1967) $\mathscr{M}(c)$ is a pentadiagonal matrix.

4. Numerical results

To solve the resultant matrix-eigenvalue problem for the complex eigenvalue c we use Osborne's (1967) iteration scheme. In this method the following iteration is implemented:

$$\mathscr{M}(c_i)\mathbf{v}_{i+1} = \frac{d\mathscr{M}(c_i)}{dc}\frac{\mathbf{u}_i}{(\mathbf{u}_i)_p}, \quad \mathscr{M}(c_i)\mathbf{u}_{i+1} = \frac{d\mathscr{M}(c_i)}{dc}\mathbf{v}_{i+1}, \tag{4.1}$$

$$c_{i+1} = c_i - (\mathbf{v}_{i+1})_p/(\mathbf{u}_{i+1})_p,$$

where $\mathbf{u}_{i+1}$ and $\mathbf{v}_{i+1}$ are vectors which should not be confused with the first-order velocity components of the previous sections. The suffix i denotes the stage of the iteration and p is the index of the component of maximum modulus in $\mathbf{u}_i$ or $\mathbf{u}_{i+1}$. In this iteration Newton's method is used to obtain the eigenvalues of the matrix $\mathscr{M}(c_i)$ and the maximum component of a vector is obtained in the direction of the eigenvector. Osborne (1967) has shown that when $\mathscr{M}$ is linear in c the iteration is of third order in the mesh spacing.

Although the Orr–Sommerfeld differential equation is linear in c, the boundary conditions at $z = 0$ introduce elements into $\mathscr{M}(c)$ which are nonlinear in c, containing factors of the form

$$\frac{a_0 + a_1(U_s - c) + a_2(U_s - c)^2 + a_3(U_s - c)^3 + a_4(U_s - c)^4}{b_0 + b_1(U_s - c) + b_2(U_s - c)^2 + b_3(U_s - c)^3 + b_4(U_s - c)^4}. \tag{4.2}$$

For the mean shear flow we have used a logarithmic–linear profile in the air and a linear–logarithmic profile in the water which are coupled at the air–water interface by matching of the mean tangential stress (Shemdin 1972). Accordingly we have set

$$\rho_a(U_*^a)^2 = \rho_w(U_*^w)^2 \tag{4.3}$$

in the specification of the mean shear profiles in both media. U_*^w is the friction velocity in the water and U_*^a is the air friction velocity, which is approximately equal to 5% of the wind speed.

To start the iteration (4.1) we let the real and imaginary parts of $\mathbf{u}_1/(\mathbf{u}_1)_p$ be unity and zero respectively at each level of z. For the initial eigenvalue we assume complete advection of the water wave by the surface drift. That is,

$$\mathrm{Re}(c_1) = \pm c_0 + U_s, \quad \mathrm{Im}(c_1) = \pm\tfrac{1}{100}(c_0 + U_s), \tag{4.4}$$

where c_0 is the classical phase speed of infinitesimal gravity–capillary waves and U_s is 3–4% of the wind speed (Wright & Keller 1971; Shemdin 1972; Keller *et al.* 1974; Wu 1975). In comparing our results with the Miles (1962*b*) predictions we let the flow inside the water vanish and, of course, for this case $U_s = 0$ also. The upper signs in (4.4) apply for a wave travelling with the wind and the lower signs apply for a wave travelling against the wind. For the lower wind speeds the choice of the initial estimate of the eigenvalue was not really all that important to convergence. For wind speeds greater than 6 m/s and wavenumbers less than 1·55 cm^{-1} an improved initial estimate of the eigenvalue hastens convergence.

Calculations with the coupled shear-flow perturbation model have been performed with a CDC 3800 computer in single-precision complex arithmetic (precision approximately ten decimal digits). Numerical results were obtained for wavenumbers between 0·628 and 8·67 cm^{-1} for wind speeds up to 15 m/s. The greatest accuracy in the numerical results was achieved for the larger wavenumbers and the small to intermediate wind speeds. The number of mesh points ranged from about 101 to 1001. Typical computation times ranged from about 1·25 s per iteration for 101 mesh points and increased linearly with the number of mesh points. In most of the computations half of the mesh points were placed in each medium.

Convergence was obtained in about three to four iterations for wind speeds less than 6 m/s. For the higher wind speeds more iterations were required and a maximum of ten was arbitrarily set. In some cases convergence did not result after ten iterations. Typically, these failures occurred for waves travelling downwind, for which the critical layer approaches the water surface (i.e. $\mathrm{Re}\,(c) \rightarrow U_s$). We believe that some of these convergence problems arise from the sensitivity of the factors (4.2) to $U_s - c$. Specifically, the real part of $U_s - c$ vanishes as the critical layer meets the interface and the imaginary part of $U_s - c$ is quite small. Our mesh size ranged from 0·04 to 0·0004 cm, and this is apparently inadequate in some cases, in particular for the larger wind speeds and the smaller wavenumbers.

The computational dilemma is as follows. One should have a $z_{\mathrm{max}} \equiv Nh$ at least as large as about a half-wavelength to obtain a sufficiently accurate phase speed. One should also have a mesh size fine enough so that an adequate number of samples exist within the critical layer of thickness $(\nu/kU')^{\frac{1}{3}}$ in order to obtain an accurate growth rate for the surface wave. Hence the accuracy of the results deteriorates for the smaller wavenumbers, since z_{max} must increase linearly with k^{-1} to obtain the correct $\mathrm{Re}\,(c)$ while to maintain the same number of points within the critical layer the mesh can only increase as $k^{-\frac{1}{3}}$. Therefore a compromise must be made to accommodate both of these requirements. When the critical layer approaches the water there is no compromise possible. For these cases what is needed is a variable-grid approach. We attempted to develop a scheme using a variable grid spacing such as that of Hughes (1972), but were unsuccessful owing to the much greater complexity of our problem.

In numerical experiments performed to increase our accuracy, Osborne's iteration scheme was used in combination with a mesh reducing procedure. In this procedure, first an appropriate z_{max} is used to obtain an accurate $\mathrm{Re}\,(c)$. Then, at the next stage the mesh size is cut in half, keeping the total number of mesh points constant. The boundary conditions at $z = \pm\frac{1}{2}z_{\mathrm{max}}$ are then obtained from the eigenfunctions just derived with the coarse mesh. The previously found eigenfunctions and eigenvalue were then used to initiate the iteration with the finer mesh (the values of the eigenfunction needed for the intermediate points of the coarse mesh are obtained by linear interpolation).

The procedure is then repeated as many times as desired, thus achieving much smaller mesh sizes. Unfortunately, in this procedure it is not possible to arrive at an unambiguous criterion for deciding on the correct eigenvalue.

In the standard Osborne iteration scheme we found that, as the number of mesh points was increased from 101 to 1001, arithmetic round-off errors became evident. This was alleviated somewhat by using the following method involving residuals to improve on the eigenvectors. After the vectors are obtained by Gaussian elimination using full-pivoting they are substituted into the original system of equations and residuals are calculated. From the residuals, corrections to the vectors are obtained at each step. This procedure improved the eigenvectors in the fifth significant figure, but the time per iteration increased by a factor of three from the standard iteration procedure.

Numerical calculations have performed for various types of logarithmic–linear profiles which are typical of turbulent flows. However, specific results will be given here only for Miles's (1962*a*) profile modified to include drift in the water. In the air the flow profile is

$$U(z) = \left\{\begin{array}{ll} U_s + U^a_* z/z^a_0 & \text{for} \quad z \leqslant z^a_1, \\ U_s + U^a_1 + 2{\cdot}5 U^a_* (\alpha_a - \tanh \tfrac{1}{2}\alpha_a) & \text{for} \quad z \geqslant z^a_1, \end{array}\right\} \tag{4.5}$$

and in the water the flow profile (in which z is taken positive into the water) is

$$U(z) = \left\{\begin{array}{ll} U_s - U^w_* z/z^w_0 & \text{for} \quad z \leqslant z^w_1, \\ U_s - U^w_1 - 2{\cdot}5 U^w_* (\alpha_w - \tanh \tfrac{1}{2}\alpha_w) & \text{for} \quad z \geqslant z^w_1, \end{array}\right\} \tag{4.6}$$

where

$$\sinh \alpha_a = (z - z^a_1)/1{\cdot}25 z^a_0, \quad \sinh \alpha_w = (z - z^w_1)/1{\cdot}25 z^w_0,$$

$$z^a_0 = \nu_a/U^a_*, \quad z^w_0 = \nu_w/U^*_w, \quad \rho_a (U^a_*)^2 = \rho_w (U^w_*)^2, \quad U^a_* = 0{\cdot}05 \times \text{wind},$$

$$\nu_a = 0{\cdot}15\,\text{cm}^2/\text{s}, \quad \nu_w = 0{\cdot}01\,\text{cm}^2/\text{s}.$$

In comparing with Miles's (1962*b*) wave growth predictions we have set $U_s = 0$ and $U(z) = U'(z) = U''(z) = 0$ in the water.

The phase speeds obtained with the coupled shear-flow model for Miles's loglin–zero profile (no flow in the water) are shown in figure 4. As expected the phase speed decreases in magnitude with increasing air friction velocity as the negative pressure produced by the mean flow in the air (i.e. inertial effect) tends to slow the wave down. It is well known that, when the phase speed of the surface wave becomes zero (i.e. the critical layer approaches the air–water interface), a Kelvin–Helmholtz instability occurs. In this figure the phase speeds for a wave travelling against the wind are also given. Upwind-travelling waves have been observed in wave tanks (J. W. Wright, private communication).

When the shear flow in the water is included the waves are also advected. The resultant phase speeds (figure 5) now are a balance of two counteracting effects: advection of the wave by the flow in the water and the inertial effect from the flow in the air. It is evident that advection predominates initially, but as the wind speed increases, the inertial effect from the flow in the air becomes significant. The reduction in phase-speed magnitude with increasing wind speed for

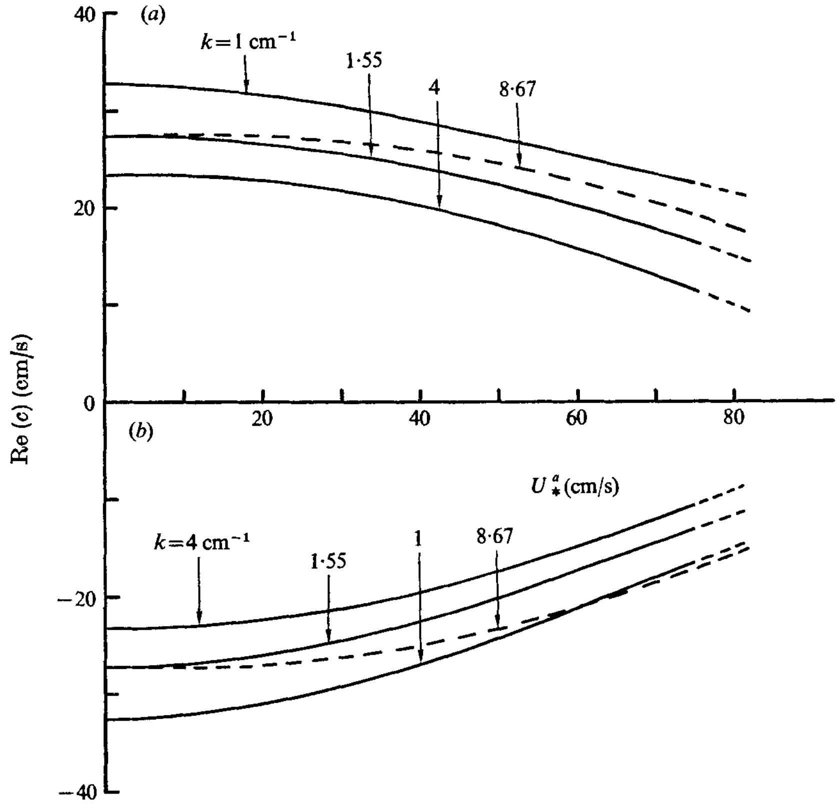

FIGURE 4. Theoretical phase speeds obtained with the coupled shear-flow model for the case of no flow in the water with a Miles (1962*a*) logarithmic–linear mean flow profile in the air. $U_1^a = 5U_*^a$, $z_0^a = \nu_a/U_*^a$, $U_s = 0$ and $U_*^a = 0{\cdot}05 \times \text{wind}$. (*a*) Wave travelling with the wind. (*b*) Wave travelling against the wind.

the small wavenumbers is also due in part to the decrease in the boundary-layer thickness in the water. In some cases the critical layer (for a wave travelling with the wind) descends towards the air–water interface and becomes submerged in the water. This descent of the critical layer may be crucial in producing larger growth rates than those predicted by Miles's (1962*b*) uncoupled model, in conformity with speculations of Keller *et al.* (1974). Phase speeds have also been obtained for other types of loglin–linlog profiles, but since the results are not very different from those in figures 4 and 5, they will not be given here.

Typical growth and damping rates obtained with the coupled shear-flow perturbation model are shown in figures 6(*a*)–(*c*). These growth rates have been obtained by multiplying the imaginary part of c by $2k$. It is evident in these figures that convergence was not possible for the smaller wavenumbers and the larger wind speeds. It is nonetheless clear that the presence of the surface drift (shear flow in the water) produces larger growth rates. Also note that the growth rates of the waves travelling with the wind are larger than the damping rates of the waves travelling against the wind.

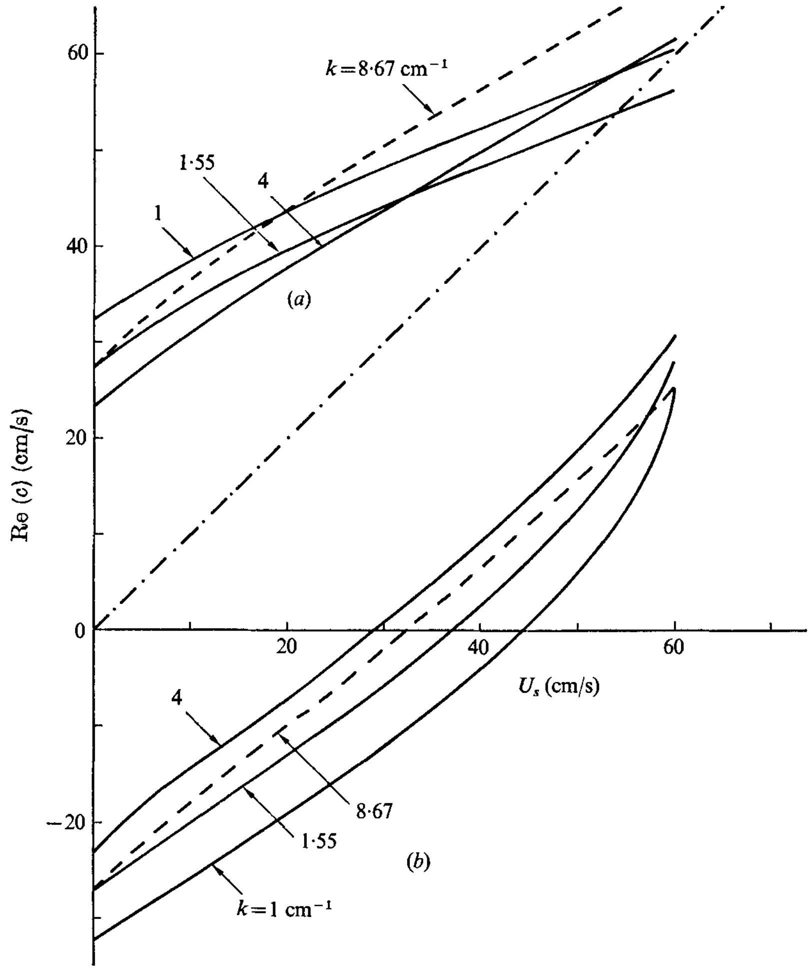

Figure 5. Theoretical phase speeds obtained with the coupled shear-flow model for the case $U_s = 0{\cdot}04 \times$ wind with a Miles (1962*a*) logarithmic–linear profile in the air and in the water. $U_1 = 5U_*$, $z_0 = \nu/U_*$, $U_*^a = 0{\cdot}05 \times$ wind and $U_*^w = U_a^*(\rho_a/\rho_w)^{\frac{1}{2}}$. (*a*) Wave travelling with the wind. (*b*) Wave travelling against the wind.

Our calculated growth rates are compared with those given by Miles (1962*b*) for $U_a^1 = 5U_*^a$ in figure 7. We have set $U_s = 0$ in (4.5) and

$$U(z) = U'(z) = U''(z) = 0$$

in the water in accordance with the assumptions of the uncoupled model, but have retained the coupling between air and water by using the exact boundary conditions for the tangential velocity and stress rather than Benjamin's (1959) approximation. This may account for the minor differences in calculated results for the shorter waves. In general our results are larger than those of Miles for the longer waves and this is presumably due to the approximations inherent in Miles's uncoupled calculation. Note also that our numerical results do not indicate the

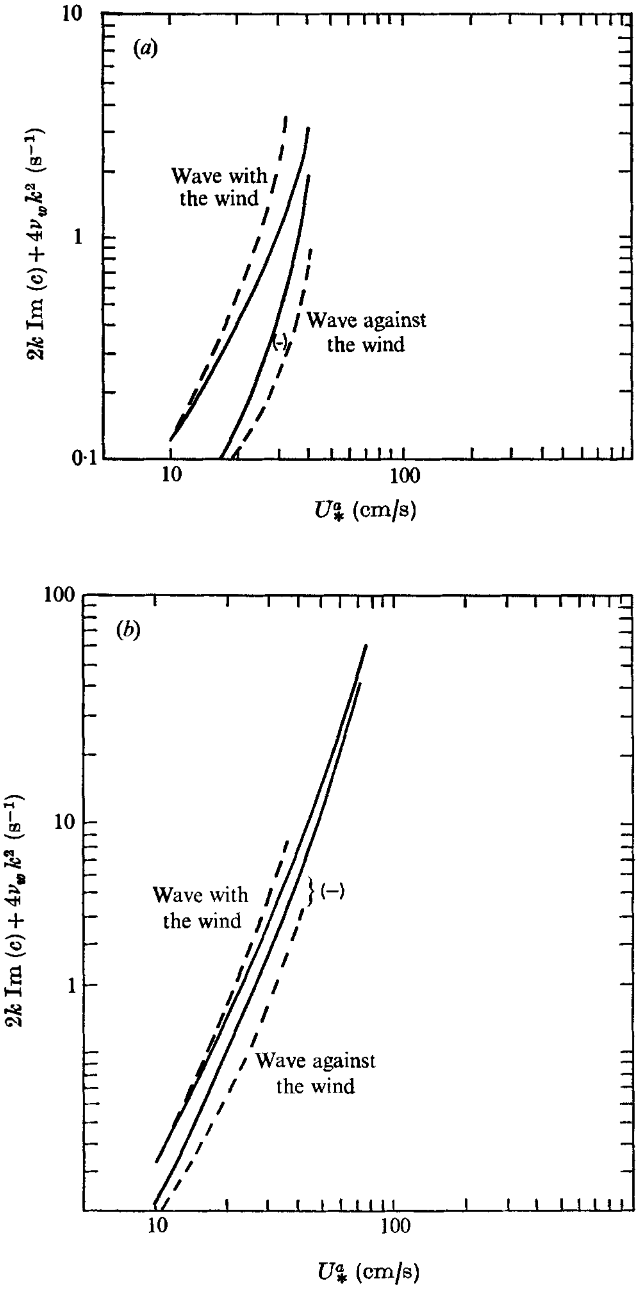

FIGURES 6 (*a*, *b*). For legend see facing page.

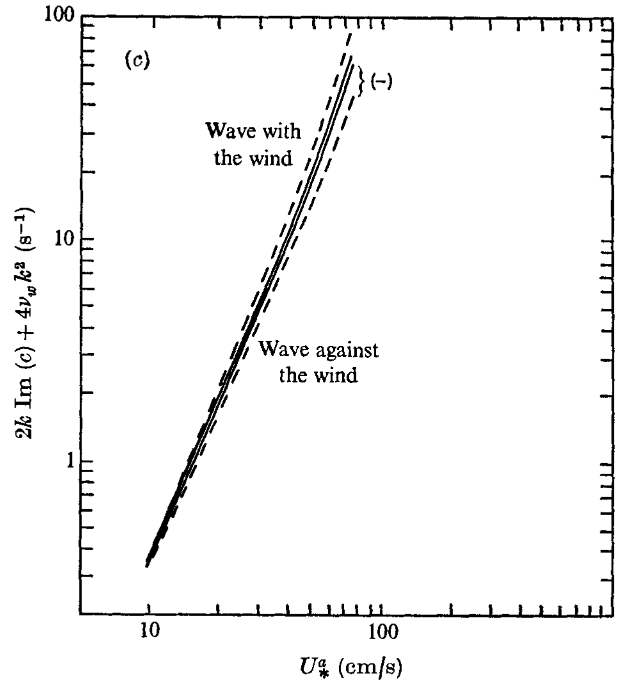

FIGURE 6. Theoretical wind-wave growth (damping) rates obtained with the coupled shear-flow model. $U_1 = 5U_*$, ——, $U_s = 0$; – – –, $U_s = 0{\cdot}04 \times$ wind. (*a*) $k = 0{\cdot}9$ cm^{-1}. (*b*) $k = 3{\cdot}4$ cm^{-1}. (*c*) $k = 8{\cdot}67$ cm^{-1}.

resonant phenomenon for $U_*^a = 6$ cm/s shown by Miles's predictions. Failure to observe such a phenomenon was a source of the scepticism of Wilson *et al.* (1973) about the applicability of Miles's (1962*b*) calculation to growth of wind-generated waves.

5. Comparison with measured growth rates

Recently Larson & Wright (1975) reported measurements of the initial temporal growth of waves in which exponential growth over several orders of magnitude in mean-square wave amplitude was observed after a wind was suddenly applied to a calm water surface. Comparison of such measurements with the results of a linear instability calculation, such as that reported here, is particularly apt. Although it can be demonstrated that the laminar sublayers will surely develop faster than the waves, we must note that the transient nature of the measurement does lead to some uncertainties on the magnitude of other pertinent parameters of the mean flow. First, the growth time of the wind drift is unknown but is probably long compared with the growth time of the shortest waves, which are less sensitive to this parameter in any case (i.e. short waves are mostly advected). The point is not as clear in the case of the longer waves, for these longer waves grow more slowly and the relevant part of the boundary layer may not develop as fast as the waves. Larson & Wright (1975), however, do report

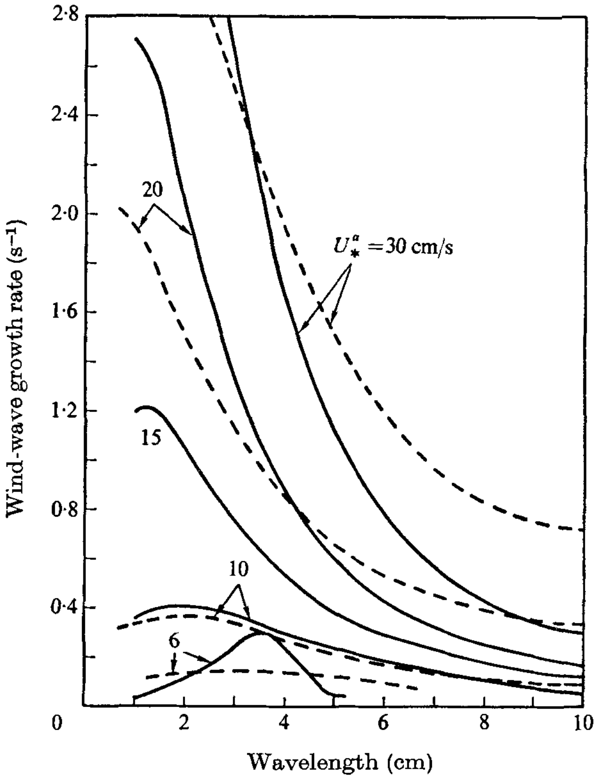

FIGURE 7. Comparison of wind-wave growth rates. – – –, from the coupled shear-flow model with $U_s = 0$; ——, Miles's (1962*b*) predictions. $U_1^a = 5U_*^a$.

that a single unambiguous exponential growth rate was observed in all cases. Thus there was no evidence of wave growth variations caused by an unsteady wind drift.

In any case, in the comparisons shown in figures 8–13, the calculated growth rates are shown both for the case of no drift and for a fully developed surface drift of 4 % of the wind. There is also an uncertainty about the appropriate value of the air friction velocity to be used in the comparison. Air friction velocities determined from logarithmic profiles in wind-wave tanks are generally closely proportional to, and about 5 % of, the wind up to air friction velocities of about 50 cm/s. At higher winds the air friction velocity increases more rapidly. Air friction velocities may also depend on fetch in wind-wave tanks (Mitsuyasu & Honda 1975). Although Larson & Wright (1975) reported no such fetch dependence for fetches greater than a metre, subsequent measurements showed a significant decrease in U_*^a at fetches shorter than a metre and winds greater than 10 m/s (J. W. Wright, private communication). It would not be surprising if both the nonlinear wind-speed dependence and fetch dependence of U_*^a were due to waves, which are, of course, absent during the initial growth measurements of Larson & Wright (1975; also see Phillips 1966, p. 141). Thus a value of U_*^a equal to 5 % of the wind speed may be more appropriate to the transient condition

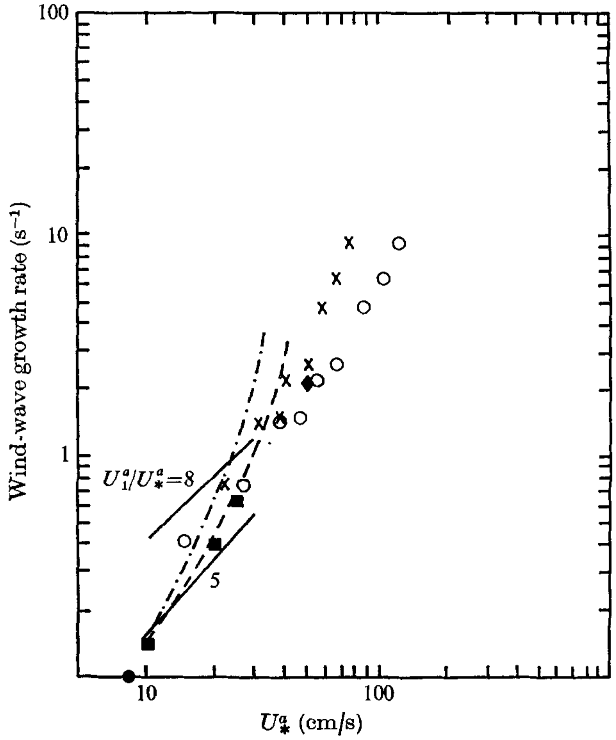

FIGURE 8. Measured and theoretical wind-wave growth rates for $k = 0\cdot9$ cm^{-1}. Theory (for $U^a_* = 0\cdot05\times$wind): ——, Miles's (1962*b*) model; – – –, this work, $U_s = 0$; —·—, this work, $U_s = 0\cdot04\times$wind. Experiment: ○, Larson & Wright, 3 m fetch; ×, Larson & Wright, measured points plotted for $U^a_* = 0\cdot05\times$wind; ■, Gottifredi & Jameson (4·61 Hz); ◆, Hidy & Plate (4 Hz); ●, Wilson *et al.* (5 Hz).

than the value measured in the steady state. In any case the measured values of the wind-wave growth rate have been plotted in figures 8–13 at values of U^a_* equal to 5 % of the wind as well as at the steady-state value. Steady-state wave growth rates reported by Hidy & Plate (1966), Gottifredi & Jameson (1970) and Wilson *et al.* (1973) have also been plotted in figures 8 and 9.

Finally Miles's (1962*b*) predictions for $U^a_1 = 5U^a_*$ and $U^a_1 = 8U^a_*$ are also shown in figures 8–13. The value $U^a_1 = 5U^a_*$ and the concomitant boundary-layer thickness, $5z^a_0$, generally give better overall agreement with the measurements and these are the values used in our calculations, as noted previously. It is also worth noting that this value of the boundary-layer thickness yields calculated phase speeds in excellent agreement (figure 14) with those determined from microwave Doppler spectra by Keller *et al.* (1974) for $k = 3\cdot4$ cm^{-1}. Although the phase speeds are not critically dependent on the boundary-layer thickness, is is nonetheless satisfying that the value of this parameter which gives the best agreement for the imaginary part of the eigenvalue also works well for the real part.

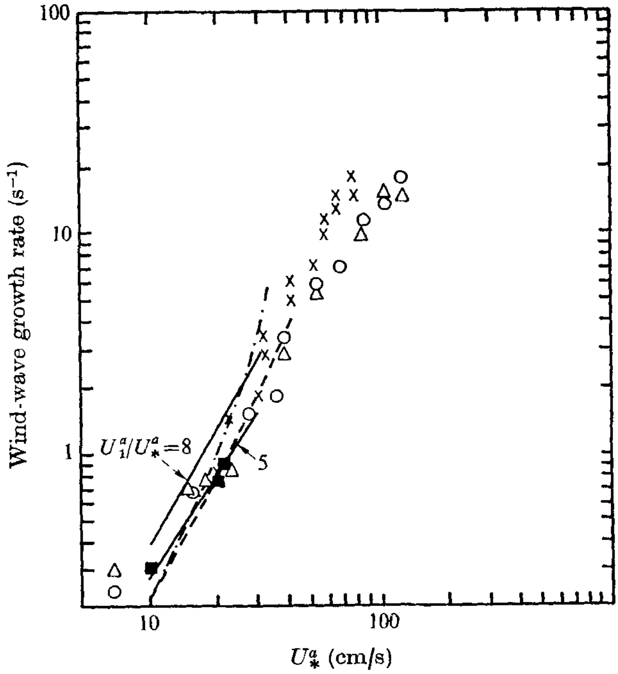

FIGURE 9. Measured and theoretical wind-wave growth rates for $k = 1{\cdot}55$ cm^{-1}. Theory (for $U^a = 0{\cdot}05 \times$ wind): ——, Miles's (1962*b*) model; – – –, this work, $U_s = 0$; —·—, this work, $U_s = 0{\cdot}04 \times$ wind. Experiment: ○, Larson & Wright, 3 m fetch; △, Larson & Wright, 8·4 m fetch; ×, Larson & Wright, measured points plotted for $U_*^a = 0{\cdot}05 \times$ wind; ■, Gottifredi & Jameson (6·2 Hz).

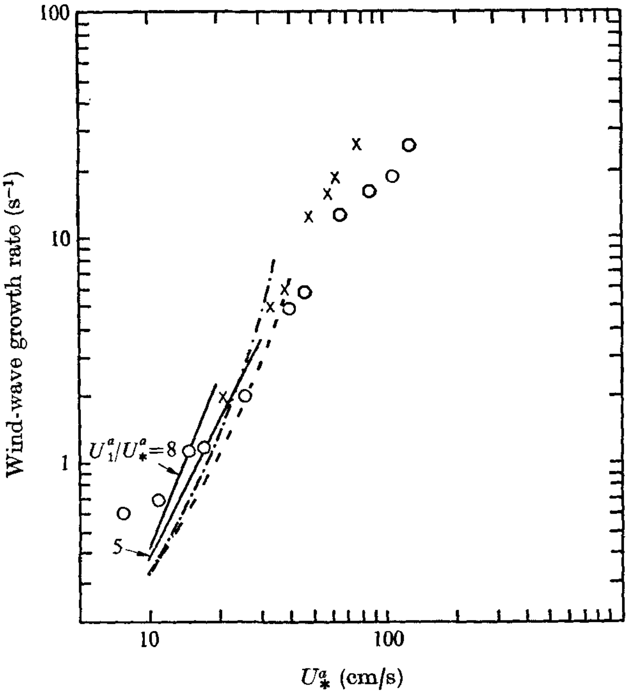

FIGURE 10. Measured and theoretical wind-wave growth rates for $k = 2{\cdot}31$ cm^{-1}. Theory (for $U_*^a = 0{\cdot}05 \times$ wind): ——, Miles's (1962*b*) model; – – –, this work, $U_s = 0$; —·—, this work, $U_s = 0{\cdot}04 \times$ wind. Experiment (Larson & Wright): ○, 3 m fetch; ×, measured points plotted for $U_*^a = 0{\cdot}05 \times$ wind.

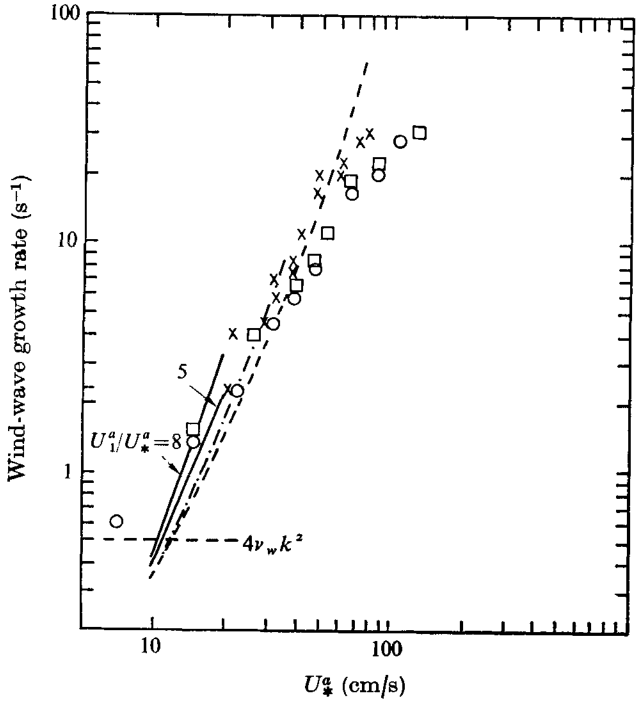

FIGURE 11. Measured and theoretical wind-wave growth rates for $k = 3{\cdot}4\ \text{cm}^{-1}$. Theory (for $U_*^a = 0{\cdot}05 \times \text{wind}$): ——— Miles's (1962*b*) model; – – –, this work, $U_s = 0$; —·—, this work, $U_s = 0{\cdot}04 \times \text{wind}$. Experiment (Larson & Wright): □, 1 m fetch; ○, 3 m fetch; ×, measured points plotted for $U_*^a = 0{\cdot}05 \times \text{wind}$.

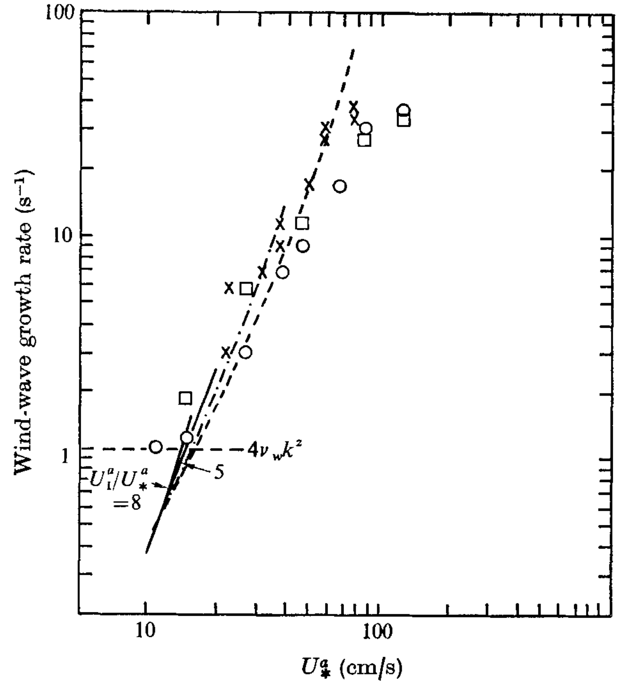

FIGURE 12. Measured and theoretical wind-wave growth rates for $k = 5{\cdot}01\ \text{cm}^{-1}$. Theory (for $U_*^a = 0{\cdot}05 \times \text{wind}$): ———, Miles's (1962*b*) model; – – –, this work, $U_s = 0$; —·—, this work, $U_s = 0{\cdot}04 \times \text{wind}$. Experiment (Larson & Wright): □, 1 m fetch; ○, 3 m fetch; ×, measured points plotted for $U_*^a = 0{\cdot}05 \times \text{wind}$.

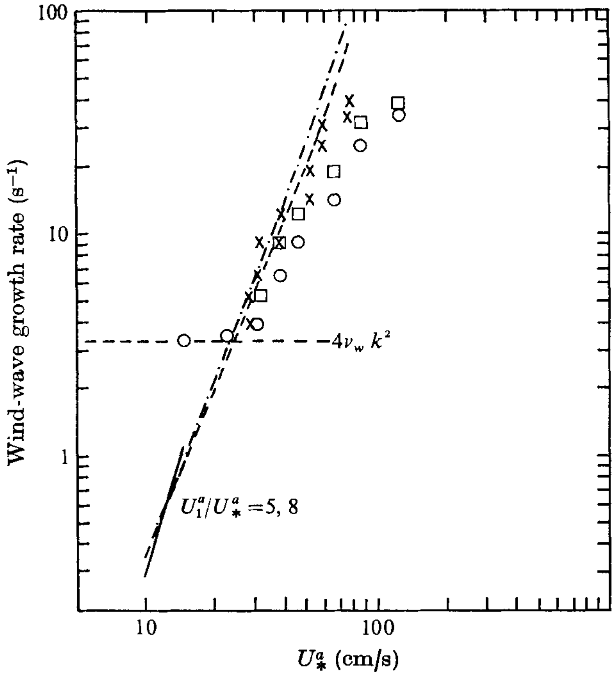

FIGURE 13. Measured and theoretical wind-wave growth rates for $k = 8{\cdot}67$ cm^{-1}. Theory (for $U_*^a = 0{\cdot}05 \times$ wind): ——, Miles's (1962*b*) model; – – –, this work, $U_s = 0$; —·—, this work, $U_s = 0{\cdot}04 \times$ wind. Experiment (Larson & Wright): □, 1 m fetch; ○, 3 m fetch; ×, measured points plotted for $U_*^a = 0{\cdot}05 \times$ wind.

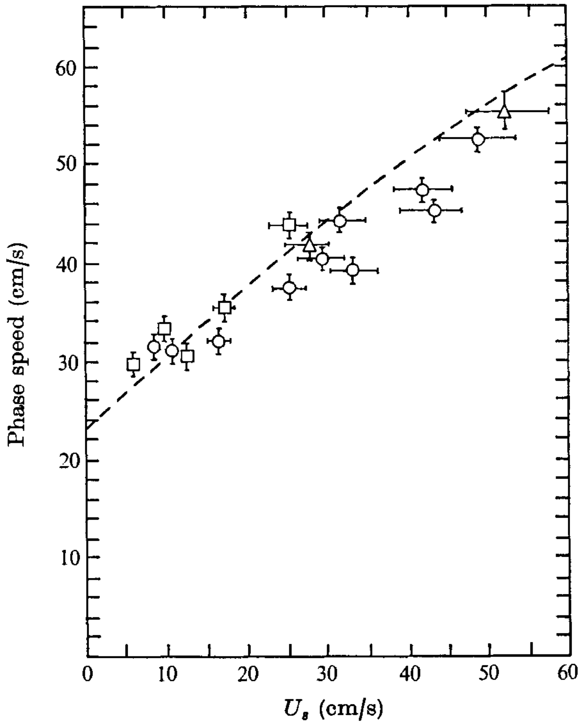

FIGURE 14. Comparison of phase speeds obtained with a coupled shear-flow model (curve, for $U_1 = 5U_*$, $U_*^a = 0{\cdot}05 \times$ wind and $U_s = 0{\cdot}04 \times$ wind) with measurements of Keller *et al.* (points) for $k = 3{\cdot}4$ cm^{-1}.

6. Conclusions

We have developed a complete viscous, linear, coupled, shear-flow perturbation model for the growth rates and phase speeds of gravity–capillary wind waves. Using finite-difference methods the boundary-value problem has been converted into a matrix-eigenvalue problem, which has been solved using Osborne's (1967) iteration scheme. The complete viscous, coupled, shear-flow model predicts waves which grow when travelling with the wind and decay when travelling against the wind.

The growth rates calculated from the model, which does not include turbulent stresses, are in reasonable agreement with the measured growth rates of gravity–capillary wind waves of Larson & Wright (1975). This implies that the growth of gravity–capillary waves is indeed due to the instability of shear flows in the air and in the water.

Comparisons of the predictions of the coupled shear-flow model for vanishing flow in the water with those by Miles's (1962*b*) model show that Miles underpredicts the growth rates of wavenumbers less than 1·55 cm^{-1} and overpredicts slightly those for the large wavenumbers for $U_1^a = 5U_*^a$.

When the shear flow in the water is included a significant increase in the growth rates is obtained, in particular for wind speeds in excess of 6 m/s.

With pleasure we thank J. W. Wright for sharing physical insight, discussing the measurements and for other valuable comments and suggestions during this research. We are also indebted to J. W. Witting for providing council and understanding on boundary layers.

REFERENCES

Benjamin, T. B. 1959 *J. Fluid Mech.* **6**, 161–205.

Gottifredi, J. C. & Jameson, G. J. 1970 *Proc. Roy. Soc.* A **319**, 373–397.

Hasselmann, K., Ross, D. B., Müller, P. & Sell, W. 1976 *J. Phys. Ocean.* (to be published).

Hasselmann, K. *et al.* 1973 *Dsche Hydrogr. Z., Suppl.* A (8°), no. 12.

Hidy, G. M. & Plate, E. J. 1966 *J. Fluid Mech.* **26**, 651–687.

Hughes, T. H. 1972 *Phys. Fluids*, **15**, 725–728.

Jordinson, R. 1970 *J. Fluid Mech.* **43**, 801–811.

Keller, W. C., Larson, T. R. & Wright, J. W. 1974 *Radio Sci.* **9**, 1091–1100.

Kurtz, E. F. & Crandall, S. H. 1962 *J. Math. Phys.* **41**, 264–279.

Larson, T. R. & Wright, J. W. 1975 *J. Fluid Mech.* **70**, 417–436.

Miles, J. W. 1957 *J. Fluid Mech.* **3**, 185–204.

Miles, J. W. 1959 *J. Fluid Mech.* **6**, 568–582.

Miles, J. W. 1962*a* *J. Fluid Mech.* **13**, 427–432.

Miles, J. W. 1962*b* *J. Fluid Mech.* **13**, 433–448.

Mitsuyasu, H. & Honda, T. 1975 *Res. Inst. Appl. Mech., Kyushu Univ., Japan*, no. 22, pp. 327–355.

Osborne. R. 1967 *SIAM J. Appl. Math.* **15**, 539–557.

Phillips, O. M. 1966 *The Dynamics of the Upper Ocean*. Cambridge University Press.

SHEMDIN, O. H. 1972 *J. Phys. Ocean.* **2**, 411–419.

STEWART, R. H. 1970 *J. Fluid Mech.* **42**, 733–754.

THOMAS, L. H. 1953 *Phys. Rev.* **91**, 780–783.

WILSON, W. S., BANNER, M. L., FLOWER, R. J., MICHAEL, J. A. & WILSON, D. G. 1973 *J. Fluid Mech.* **58**, 435–460.

WRIGHT, J. W. & KELLER, W. C. 1971 *Phys Fluids*, **14**, 466–474.

WU, J. 1975 *J. Fluid Mech.* **68**, 49–70.